

# MultiDIC: an Open-Source Toolbox for Multi-View 3D Digital Image Correlation

Solav Dana<sup>1</sup>, (Member, IEEE), Moerman M. Kevin<sup>1</sup>, (Member, IEEE), Jaeger M. Aaron<sup>1</sup>,  
Genovese Katia<sup>2</sup>, and Herr M. Hugh<sup>1</sup>, (Member, IEEE)

<sup>1</sup>MIT Media Lab, Massachusetts Institute of Technology, Cambridge, MA 02139, USA

<sup>2</sup>School of Engineering, University of Basilicata, Potenza 85100, Italy

Corresponding author: Solav Dana (e-mail: danask@mit.edu).

This work was partially supported by the NIH grant no. 1R01EB024531-01. The work of Solav Dana was partially supported by the MIT-Technion postdoctoral fellowship.

**ABSTRACT** Three-dimensional Digital Image Correlation (3D-DIC) is a non-contact optical-numerical technique for evaluating the dynamic mechanical behavior at the surface of structures and materials, including biological tissues. 3D-DIC can be used to extract shape and full-field displacements and strains with high resolution, at various length scales. While various commercial and academic 3D-DIC software exist, the field lacks 3D-DIC packages which offer straight-forward calibration and data-merging solutions for multi-view analysis, which is particularly desirable in biomedical applications. To address these limitations, we present MultiDIC, an open-source MATLAB toolbox, featuring the first 3D-DIC software specifically dedicated to multi-view setups. MultiDIC integrates robust two-dimensional subset-based DIC software with specially tailored calibration procedures, to reconstruct the dynamic behavior of surfaces from multiple stereo-pairs. MultiDIC contains novel algorithms to automatically merge meshes from multiple stereo-pairs, and to compute and visualize 3D shape and full-field motion, deformation, and strain. User interfaces provide capabilities to perform 3D-DIC analyses without interacting with MATLAB syntax, while stand-alone functions also allow proficient MATLAB users to write custom scripts for specific experimental requirements. This paper discusses the challenges underlying multi-view 3D-DIC, details the proposed solutions, and describes the algorithms implemented in MultiDIC. The performance of MultiDIC is tested using a low-cost experimental system featuring a 360° twelve-camera setup. The software and system are evaluated using measurement of a cylindrical object with known geometry subjected to rigid body motion and measurement of the lower limb of a human subject. The findings confirm that shape, motion, and full-field deformations and strains can be accurately measured, and demonstrate the feasibility of MultiDIC in multi-view *in-vivo* biomedical applications.

**INDEX TERMS** Biomedical Image Analysis, Full-field 3D Deformation, Material Mechanical Properties, Open Source Software, Skin Shape and strain, Soft Tissue Biomechanics, Stereo-DIC, Strain map.

## I. INTRODUCTION

Digital Image Correlation (DIC) is a full-field non-contact optical-numerical technique to measure shape, motion, and deformation, on almost any kind of material, even in extreme experimental settings, as long as the region of interest (ROI) on the sample's surface is provided with a natural or synthetic speckle pattern [1], [2]. This allows the DIC algorithm to match dense sets of corresponding points in different images of the ROI, based on the local pixel intensity distribution. Specifically, local two-dimensional DIC (2D-DIC) [2] defines a pixel subset around a point of interest in a reference image and evaluates the parameters describing its motion and deformation in a given target image. In Three-dimensional DIC (3D-DIC), two cameras view an ROI from different angles (i.e. a stereo-camera pair), and capture a sequence of images representing a reference configuration (typically an undeformed configuration) and a required number of "current" configurations (typically deformed configurations). Next, 2D-DIC is used to correlate a given set of points in the two stereo-views of the reference configuration (spatial correlation) and track these points throughout the sequence of stereo-images representing the current configurations (temporal correlation). The correlated sets of image points are then used to reconstruct and track the 3D position of the material points of the ROI over time, via stereo-triangulation [1], [3].

DIC was originally developed for experimental mechanics, where it has become a standard technique for characterizing material properties and the response of structures to loads [4]. The non-contact, full-field, and large deformation capabilities of DIC make

it particularly suited for shape and deformation measurements for a wide range of biomedical applications [5]–[11]. DIC methods have been used in combination with advanced inverse characterization methods to identify the mechanical properties of natural and synthetic biological materials and body parts [5]–[8].

Substantial work has been done in recent decades to improve the performance of computational algorithms [12]–[17], to define good practices for performing experiments and calibration [18], to assess the measurement errors [19], [20], and to extend the capabilities of 3D-DIC [15], [21]. Furthermore, various commercial and academic software packages now exist. However, there is currently a lack of available 3D-DIC software specifically tailored for multi-view analysis, a feature which is highly desirable for biomedical applications. It is challenging to study the shape, motion, and deformation of tissues and organs *in-vivo*, due to the often complex geometries, the large deformations that can occur, and the risk of undesired motions. To overcome these challenges, simultaneous multi-view imaging is often utilized [11], [22]. Moreover, in a clinical environment, a fast and flexible image acquisition and calibration process is highly desirable [23].

Several multi-view DIC systems have been proposed in the literature (e.g. [22], [24]–[29]), where multiple cameras with partially overlapping fields of view (FOVs) allow for the imaging of large portions of an object surface. The multitude of cameras can be arranged in a 2D array when large quasi-planar objects need to be measured. Alternatively, for non-planar objects, the set of cameras are placed around the object, e.g. in a surrounding fashion, to obtain the 3D shape of the entire object (as illustrated in Fig. 1). In this work, we refer to the latter configuration, which is suitable for many biomedical applications.

Furthermore, in scientific research reproducibility, verifiability, and validation are key [30]. Only open-source software tools offer full insight into the computational framework these aspects demand. Moreover, open-source software enable customizability, which is important since each scientific application offers its own unique computational and experimental challenges. There is hence a pressing need for open-source software implementing algorithms specifically tailored for multi-view 3D-DIC, which allow for customization and easy adaptation to different experimental settings.

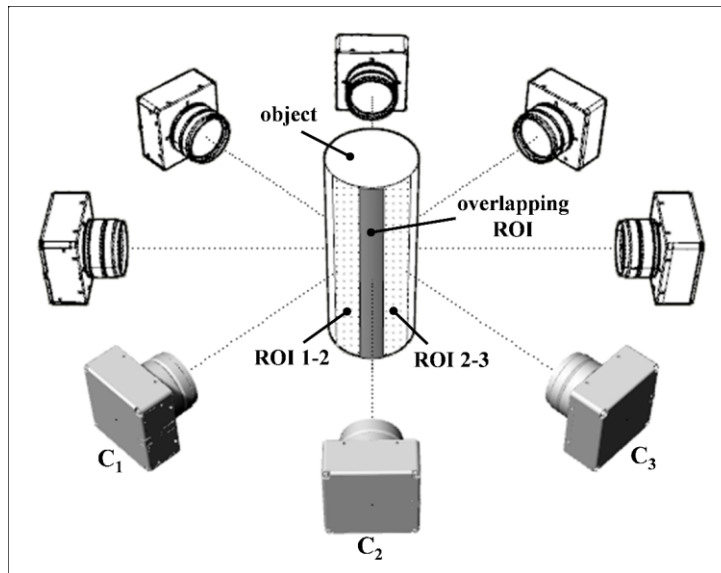


**FIGURE 1.** Multi-view stereo system schematic. A circular array of cameras (in transparent color) surrounding the object, with highlighted two contiguous stereo-pairs (in solid color), sharing a common field of view on the object’s surface. The ROI for each pair is depicted on the object’s surfaces with dots, and the overlapping ROI for the two pairs is depicted with solid color.

### A. THEORETICAL BACKGROUND

Two key issues entailed in the implementation of multi-view setups are system calibration (required for stereo triangulation) and data merging (required for combining results from multiple stereo-pairs). For each camera of a typical stereo-pair, calibration aims to find the intrinsic parameters (defining the geometric and optical characteristics of the camera) and the extrinsic parameters (defining the position and orientation of the camera with respect to a reference coordinate system). Together, the intrinsic and extrinsic parameters serve to describe the transformation that maps each 3D material point  $\mathbf{P}(X, Y, Z)$  in the global coordinate system into its image point on the camera sensor  $I(x_p, y_p)$ , according to the pinhole optical model [3], [31]. Specifically, the coordinates  $(X, Y, Z)$  are first rigidly transformed into the coordinates  $(X_C, Y_C, Z_C)$  in the camera coordinate system by

$$\begin{bmatrix} X_C \\ Y_C \\ Z_C \end{bmatrix} = \begin{bmatrix} R_{11} & R_{12} & R_{13} \\ R_{21} & R_{22} & R_{23} \\ R_{31} & R_{32} & R_{33} \end{bmatrix} \begin{bmatrix} X \\ Y \\ Z \end{bmatrix} + \begin{bmatrix} T_x \\ T_y \\ T_z \end{bmatrix}, \quad (1)$$

where  $R_{ij}$  ( $i, j = 1, 2, 3$ ) and  $T_x, T_y, T_z$  are the components of the rotation matrix and the translation vector, respectively. Next, the (ideal) normalized image point coordinates are calculated as

$$x = X_C/Z_C ; \quad y = Y_C/Z_C. \quad (2)$$

Then, the intrinsic camera parameters, i.e. the focal lengths in pixels  $[f_x, f_y]$ , the principal point (optical center) coordinates  $[C_x, C_y]$ , and the skew coefficient  $s = f_y \tan \alpha$ , where  $\alpha$  is the angle between the horizontal and vertical axes of the sensor ( $\alpha = s = 0$  if the axes are perpendicular), are used to calculate the image point coordinates  $I(x_p, y_p)$ , in the sensor coordinate system, by

$$\begin{bmatrix} x_p \\ y_p \\ 1 \end{bmatrix} = \begin{bmatrix} f_x & s & C_x \\ 0 & f_y & C_y \\ 0 & 0 & 1 \end{bmatrix} \begin{bmatrix} x \\ y \\ 1 \end{bmatrix}. \quad (3)$$

Next, combining Eq. (1)-(3) and further assuming that  $s = 0$  yields to

$$\begin{aligned} x_p &= f_x \frac{R_{11}X + R_{12}Y + R_{13}Z + T_x}{R_{31}X + R_{32}Y + R_{33}Z + T_z} + C_x \\ y_p &= f_y \frac{R_{21}X + R_{22}Y + R_{23}Z + T_y}{R_{31}X + R_{32}Y + R_{33}Z + T_z} + C_y, \end{aligned} \quad (4)$$

which can be rearranged into the form

$$\begin{aligned} x_p &= \frac{L_1X + L_2Y + L_3Z + L_4}{L_9X + L_{10}Y + L_{11}Z + 1} \\ y_p &= \frac{L_5X + L_6Y + L_7Z + L_8}{L_9X + L_{10}Y + L_{11}Z + 1}. \end{aligned} \quad (5)$$

Eq. (5) represents the basis of the Direct Linear Transformation (DLT) method [31] which allows for implicit camera calibration. The DLT method derives the (unphysical) parameter set  $L_j$  ( $j = 1, 2, \dots, 11$ ) by solving a linear system of equations, based on a *single* image containing a non-planar set of calibration points whose positions  $(X, Y, Z)$  are known with high accuracy. DLT, however, relies on an idealized distortion-free camera model which might yield inaccurate results, especially when high-distortion or low-quality lenses are used.

The most common stereo calibration technique used in 3D-DIC methods is the Bundle Adjustment (BA) method [1]. BA is an explicit calibration method that allows for the estimation of both the intrinsic and extrinsic camera parameters by using repetitive observations of sparse scene points in different viewing directions [32]. BA allows for lens distortion correction based on a non-linear distortion model. Specifically, the idealized image point coordinates  $(x, y)$  in Eq. (3), are replaced by the distorted normalized coordinates  $(x_d, y_d)$  defined by

$$\begin{aligned} \begin{bmatrix} x_d \\ y_d \end{bmatrix} &= (1 + k_1r^2 + k_2r^4 + k_3r^6) \begin{bmatrix} x \\ y \end{bmatrix} \\ &+ \begin{bmatrix} 2p_1xy + p_2(r^2 + 2x^2) \\ p_1(r^2 + 2y^2) + 2p_2xy \end{bmatrix}, \end{aligned} \quad (6)$$

where  $r^2 = x^2 + y^2$ ,  $[k_1, k_2, k_3]$  are the radial distortion parameters,  $[p_1, p_2]$  are the tangential distortion parameters, and the skew parameter in (3) can be non-zero.

Successful BA typically requires a *large number* of images (approximately 50 [33]) of a planar calibration target acquired in different orientations and positions in the field of view (FOV) of both cameras. Although BA is highly accurate, and is typically the first choice for calibrating a two-camera system, the associated practice of calibrating one camera with respect to a given ‘master’ camera can limit its applicability to multi-view stereo systems. To calibrate a large number of camera-pairs, each camera-pair has to be calibrated separately. Then, the images of a given set of markers [27], or of a speckled surface [34], which can be

viewed by each contiguous pair of cameras, are used to: 1) find the geometric transform between the pairs, and 2) combine the data into a mutual coordinate system [34]. This process must be repeated for each additional camera-pair [34]. Clearly, this approach is very time-consuming, especially in case a large number of cameras is required or when the camera poses change during a data collection session, potentially causing error accumulation. Furthermore, this method does not enable combining data from camera-pairs for which the FOV do not overlap.

In contrast, the DLT method can use a *single* image acquisition of a 3D (non-planar) calibration target placed in the scene, captured by all the cameras of the multi-view system. This arrangement allows one to calibrate each camera with respect to a common reference system associated to the 3D target, thus enabling an automatic data merging, even in cases where the FOV of different camera-pairs do not overlap. The main limitation of this approach is that the calibration target usually covers only a portion of the working volume and this may affect the accuracy of the calibration results, even when distortion correction procedures are adopted [35]–[37].

## **B. OVERVIEW OF THE CURRENT WORK**

A specific aim of this work was to overcome the above-mentioned limitations of existing multi-view methods. To this end, we present MultiDIC, a free open-source software library for analyzing multi-view stereo images and obtaining 3D shapes and full-field displacements, deformations, and strains. Specific consideration is given to develop a procedure for multi-view stereo calibration and data merging, which enables camera poses to be changed as needed, without requiring a long re-calibration process.

MultiDIC utilizes the high-quality open-source 2D-DIC software Ncorr [38], which was previously verified and validated by processing standard sets of synthetic and experimental images [18]. In the present study, a combined approach for calibration was developed, whereby both BA and DLT are used in different steps, to harness the advantages of each method. Particularly, BA is used for obtaining the distortion and skew parameters, which can be used to correct the effect of distortion on the image points extracted from both the stereo calibration images and the speckled object images. BA is only required once per camera, as long as the camera's internal settings remain unaltered. DLT is then used on the undistorted image points for retrieving the internal (distortion-free) and external (camera pose) parameters of the cameras, combined into the DLT parameters. The DLT parameters refer to a common global coordinate system associated with the 3D calibration object, which is seen simultaneously from all the cameras. Since only a *single* image per camera is required, DLT can also be used to check the stability of the system whenever experiments are prolonged in time, and to quickly re-calibrate the system in case cameras are intentionally or accidentally moved. Moreover, this rationale allows one to eventually keep the original images and skip the distortion correction step in cases where images are obtained with high quality optics and sensors [25], or if the distortions are known to be negligible with respect to the required precision for the specific application.

When a large number of views is required, as is often the case in biomedical applications, imaging systems can become prohibitively expensive. In this study, we present an inexpensive system using low-cost camera modules, with which we test the capabilities of the toolbox. This paper describes the workflow of MultiDIC, the algorithms implemented in it, the experimental setup, and the data analysis procedures. Then, results of several tests that both validate it and showcase its capabilities are reported and discussed. Finally, measurement on the lower limb of a human subject demonstrates the typical shape and deformation information obtainable for *in-vivo* studies.

## **II. MATERIALS AND METHODS**

### **A. OVERVIEW OF SOFTWARE ARCHITECTURE AND ALGORITHMS**

MultiDIC is an open-source (Apache 2.0 licensed) library written in MATLAB (R2017b, The Mathworks Inc., USA), a programming language widely used among engineers and scientists. Users may visit the GitHub repository (<http://www.github.com/MultiDIC>) to obtain the most recent version (this paper refers to release version v1.0, which is also archived at <http://doi.org/10.5281/zenodo.1256041>), to join development, and to post issues. The toolbox is accompanied by a comprehensive instruction manual and sample data.

MultiDIC was designed as a flexible library of functions and scripts that users can freely adjust to fit their experimental requirements. The implementation as a toolbox enables users to perform 3D-DIC analyses and to visualize the results using user interfaces (UIs) which do not require interaction with MATLAB syntax. As such, these UIs provide access to the most common functionality as well as usability for non-code experts. For customization, proficient MATLAB users can also use the stand-alone functions and data-structures to write custom scripts and analyze large data-sets semi-automatically. Moreover, users are encouraged to extend the toolbox's functionality by implementing additional algorithms.

MultiDIC integrates the 2D-DIC open-source software Ncorr [38] with the BA algorithm included in the MATLAB computer vision toolbox [39], and the DLT algorithm implemented in MATLAB by the authors, to perform the reconstruction of 3D surfaces from multiple stereo-image pairs. Moreover, it contains algorithms for merging surfaces, and for computing full-field 3D displacements, deformations, strains, and rigid-body motion (RBM). In addition, extensive plotting and visualization functions are offered, which integrate tools from the open-source GIBBON toolbox [40].

Fig. 2 outlines the workflow of the entire 3D-DIC procedure. In the optional step 0, the distortion and skew parameters are calculated using BA on multiple images of a flat checkerboard pattern. These parameters can be used to correct for the effect of distortion on the points detected on both the calibration object images and the speckled object images. Step 1 comprises the calculation of the DLT calibration parameters of each camera, using images of a 3D calibration object seen simultaneously from all the views. Step 2 involves matching corresponding points on sets of stereo images of the speckled object using 2D-DIC. In step 3, the calibration parameters from step 1 are used to perform a stereo-triangulation which transforms the 2D points matched in step 2 for each stereo-pair into 3D triangular meshes. Furthermore, this step may optionally involve the merging together of multiple obtained surfaces. Lastly, step 4 includes algorithms for computation and visualization of the full-field displacement, deformation, strain, and RBM. The methods implemented in each of these steps are detailed in the next sub-sections.

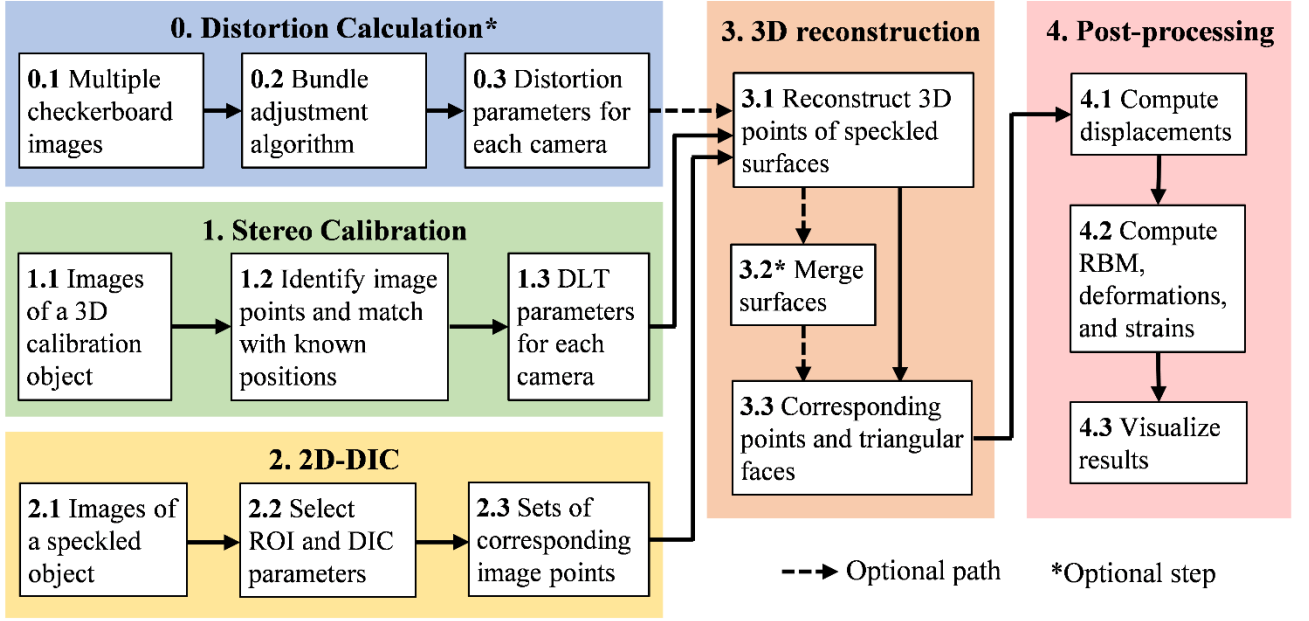


**FIGURE 2.** MultiDIC algorithm workflow. Step 0 is optional, and is only required if distortion correction is necessary. Step 1 and 2 and 3 comprise the core components of the 3D-DIC process. Moreover, step 3.2 is optional, and is only required if merging of surfaces into one continuous mesh is desired.

### B. DISTORTION CORRECTION

The purpose of this step is to find the parameters for correcting the lens distortions and skew affecting the acquired images. This step has to be executed only once per camera and needs not be repeated if a camera pose is changed, as long as the camera's intrinsic parameters remain unaltered. The MATLAB Camera Calibration Toolbox [39] was utilized, which is based on previous works [35], [41]–[43] for evaluating the camera intrinsic parameters, including distortion parameters, using the BA method. Specifically, multiple images of a planar checkerboard pattern are acquired by each camera. Then, the algorithm utilizes BA to minimize the overall re-projection errors of the corner points of the checkerboard pattern. The implemented model allows for the computation of up to six parameters: three for radial distortion, two for tangential distortion, and one for skew, as detailed in Eq. (3) and (6). These parameters are later used before the 3D reconstruction in step 3, to correct the points detected on both the stereo calibration images and the speckle images.

### C. STEREO CALIBRATION

In this step, the mapping between 2D image points and 3D world points is established, using Eq. (5). Since each control point provides two equations, a minimum of six points is required to obtain the set of 11 DLT parameters. Nevertheless, a greater number of points is preferred, as the effect of experimental errors is reduced by solving an overdetermined system through least-squares minimization.

In practice, this step requires a 3D (non-planar) calibration object having control points whose 3D positions are known with sufficient accuracy. The use of a 3D object with axial-symmetry (a cylinder in the current study) represents the optimal solution for a 360° multi-view system, since images of the calibration object can be acquired from all cameras simultaneously. The calibration images are then analyzed using MultiDIC to detect the image points  $(x_p, y_p)$  corresponding to the calibration object's

control points, and to sort and match them with their known 3D positions  $(X, Y, Z)$ . Next, the DLT parameters  $L_j$  ( $j = 1, 2, \dots, 11$ ) and the associated reconstruction errors are calculated and plotted.

#### D. 2D-DIC OF STEREO IMAGE PAIRS

In this step, which has to be conducted for each camera-pair, corresponding image points are detected using 2D-DIC, on sets of images of a speckled object acquired from two angled views, as illustrated in Fig. 3. First, a reference image is selected, typically the image acquired in the undeformed configuration from either one of the views. Second, a ROI is selected, which corresponds to an area of the object which is visible from both views. Third, a point grid is obtained inside the ROI according to selected subset size and spacing, and the corresponding points are detected on all the remaining images using Ncorr [38]. Ncorr is an open-source subset-based 2D-DIC software, described in detail in [38] together with validation results of its metrological performances tested with images from the 2D-DIC-Challenge [18]. Briefly, Ncorr implements a first order shape function to describe the pixel subset transformation [2], the least-square correlation criterion  $C_{LS}$  as a correlation cost function [38], the Inverse Compositional Gauss-Newton method as a nonlinear optimizer [44], and the Reliability-guided method [45] to propagate the analysis over the ROI, starting from user-defined seed points.

Moreover, a triangular mesh is defined on the point grid and saved for the 3D reconstruction step. Specifically, MultiDIC's step 2 serves as a wrapper for Ncorr, which allows users to select camera-pairs for analysis and draw the ROI. These data are automatically transferred into Ncorr for further analysis, and the corresponding image points, together with the associated correlation coefficients [38] are returned for defining the triangular mesh, for plotting the results, and for saving the variables necessary for 3D reconstruction.

Fig. 3 illustrates how Ncorr was able to obtain high correlation accuracy (low values of  $C_{LS}$ ) over most of the selected ROI with exception of the right border, where the affine function could not accurately describe the subset transformation in this portion of the surface [46]. In this work, a sufficiently large number of cameras (i.e. narrow ROI for each camera pair) were chosen to ensure high accuracy correlation, even on complex shapes.

#### E. 3D RECONSTRUCTION

In this step, the sets of DLT parameters  $L_j^{C_k}$  and  $L_j^{C_l}$  ( $j = 1, 2, \dots, 11$ ) associated with the cameras  $C_k$  and  $C_l$  ( $k$  and  $l$  represent the indices of the cameras in a specific stereo-pair), are used to transform each pair of corresponding image points, from their image coordinates  $(x_p^{C_k}, y_p^{C_k})$  and  $(x_p^{C_l}, y_p^{C_l})$ , into the 3D coordinates  $(X, Y, Z)$ , by rearranging Eq. (5) into the form

$$\mathbf{U} = \mathbf{A}\mathbf{P}, \quad (7)$$

where

$$\mathbf{U} = \begin{bmatrix} x_p^{C_k} - L_4^{C_k} \\ y_p^{C_k} - L_8^{C_k} \\ x_p^{C_l} - L_4^{C_l} \\ y_p^{C_l} - L_8^{C_l} \end{bmatrix}; \quad \mathbf{P} = \begin{bmatrix} X \\ Y \\ Z \end{bmatrix};$$

$$\mathbf{A} = \begin{bmatrix} L_1^{C_k} - L_9^{C_k} x_p^{C_k} & L_2^{C_k} - L_{10}^{C_k} x_p^{C_k} & L_3^{C_k} - L_{11}^{C_k} x_p^{C_k} \\ L_5^{C_k} - L_9^{C_k} y_p^{C_k} & L_6^{C_k} - L_{10}^{C_k} y_p^{C_k} & L_7^{C_k} - L_{11}^{C_k} y_p^{C_k} \\ L_1^{C_l} - L_9^{C_l} x_p^{C_l} & L_2^{C_l} - L_{10}^{C_l} x_p^{C_l} & L_3^{C_l} - L_{11}^{C_l} x_p^{C_l} \\ L_5^{C_l} - L_9^{C_l} y_p^{C_l} & L_6^{C_l} - L_{10}^{C_l} y_p^{C_l} & L_7^{C_l} - L_{11}^{C_l} y_p^{C_l} \end{bmatrix}. \quad (8)$$

Then, the least-squares solution for  $\mathbf{P}$  is obtained by

$$\mathbf{P} = [\mathbf{A}^T \mathbf{A}]^{-1} \mathbf{A}^T \mathbf{U}. \quad (9)$$

Consequently, a 3D point cloud is obtained from each stereo-pair. Since the coordinates of the control points on the calibration are expressed in the global coordinate system for all camera-pairs, all point clouds are automatically reconstructed in the global coordinate system, without the need to perform any additional coordinate transformation procedure.

Moreover, each set of  $N$  reconstructed points coordinates  $[X_n, Y_n, Z_n]$  ( $n = 1, 2 \dots N$ ) on the calibration object, and the associated true coordinates  $[X_n^{(t)}, Y_n^{(t)}, Z_n^{(t)}]$  can be used to calculate the reconstruction errors  $[\Delta X_n, \Delta Y_n, \Delta Z_n]$  as

$$\Delta X_n = X_n - X_n^{(t)}; \Delta Y_n = Y_n - Y_n^{(t)}; \Delta Z_n = Z_n - Z_n^{(t)}. \quad (10)$$

Then, the mean error  $\varepsilon_M$  and the root mean square (RMS) error  $\varepsilon_R$  are defined as

$$\varepsilon_M = \frac{1}{N} \sqrt{\left(\sum_{n=1}^N \Delta X_n\right)^2 + \left(\sum_{n=1}^N \Delta Y_n\right)^2 + \left(\sum_{n=1}^N \Delta Z_n\right)^2};$$

$$\varepsilon_R = \sqrt{\frac{1}{N} \sum_{n=1}^N (\Delta X_n)^2 + (\Delta Y_n)^2 + (\Delta Z_n)^2}. \quad (11)$$

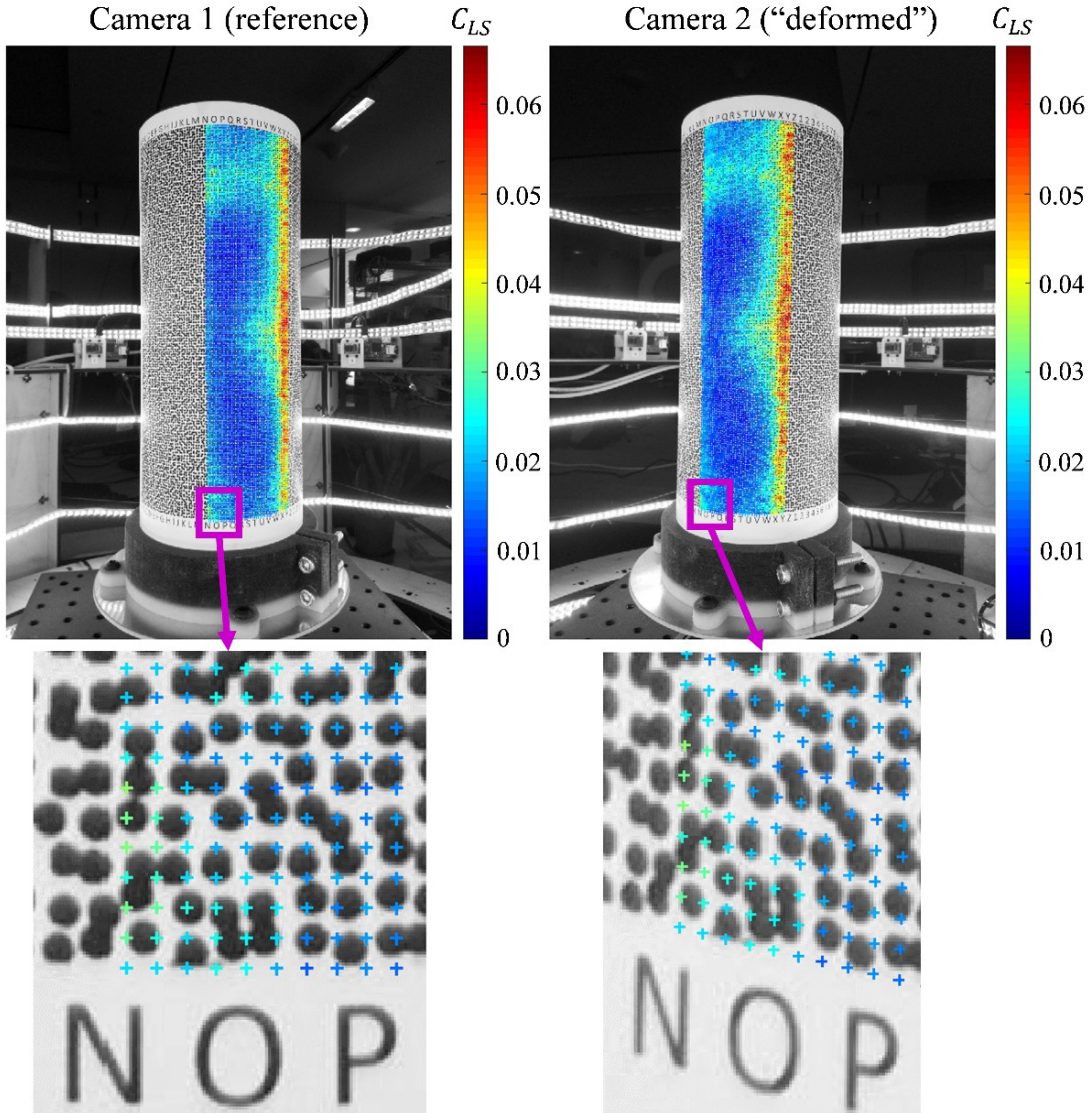


**FIGURE 3.** Point matching of stereo images using 2D-DIC. Portions of a speckled cylindrical object imaged by cameras positioned with an angular displacement of  $30^\circ$  between them are shown. The corresponding image points detected using DIC inside the ROI are shown on the reference (left) and “current” (right) images, with colors depicting the values of the correlation coefficient.

## F. SURFACE MERGING

The tessellation defined in step 2 is used here to form sets of 3D triangular meshes. The meshes obtained from each camera pair are independent, not connected to each other, and may locally overlap. In order to construct a single continuous and merged surface, the overlap between meshes needs to be resolved and adjacent meshes should be stitched together. An example schematic for resolving the overlap and for merging two adjacent surfaces is shown in Fig. 4.

To resolve the overlap, an algorithm was developed, whereby redundant faces are iteratively removed from the boundaries of overlapping regions until a user-defined minimum gap exists between the meshes. The following heuristics are employed to select which faces to remove:

1. The correlation coefficient  $C_{LS}$ , representing the matching quality of each vertex (removing vertices with poorer correlation first).
2. The distance between the meshes in the overlap region (removing faces having larger distance to the other mesh first).
3. The difference in the local orientation between the meshes in the overlap region (removing faces having larger angular displacement from the other mesh first).
4. A combination of 1, 2, and 3, with optional weights.

Once the overlap is resolved, as depicted in Fig. 4(b), the meshes are merged by introducing new faces along the gap, connecting original vertices from both meshes, as depicted in Fig. 4(c). The algorithm uses only vertices which exist in the original data. Introduction of new vertices which do not originate from an actual measurement is not desirable, since these vertices cannot be tracked in the deformed configurations and cannot provide reliable displacement and strain measurements. Moreover, keeping all the points and re-meshing the overlapping regions is not preferred because it results in a denser and often lower quality mesh, and might result in a jagged surface in regions where the two surfaces could not accurately merge. Stitching of the gap is performed by locally applying Delaunay triangulation between the vertices on the boundaries of the meshes, which maximizes the minimum angle of the triangles and ensures that quality triangles are formed. Figure 4 demonstrates how overlapping triangular meshes are successfully merged using the original vertices only, despite having different element sizes.

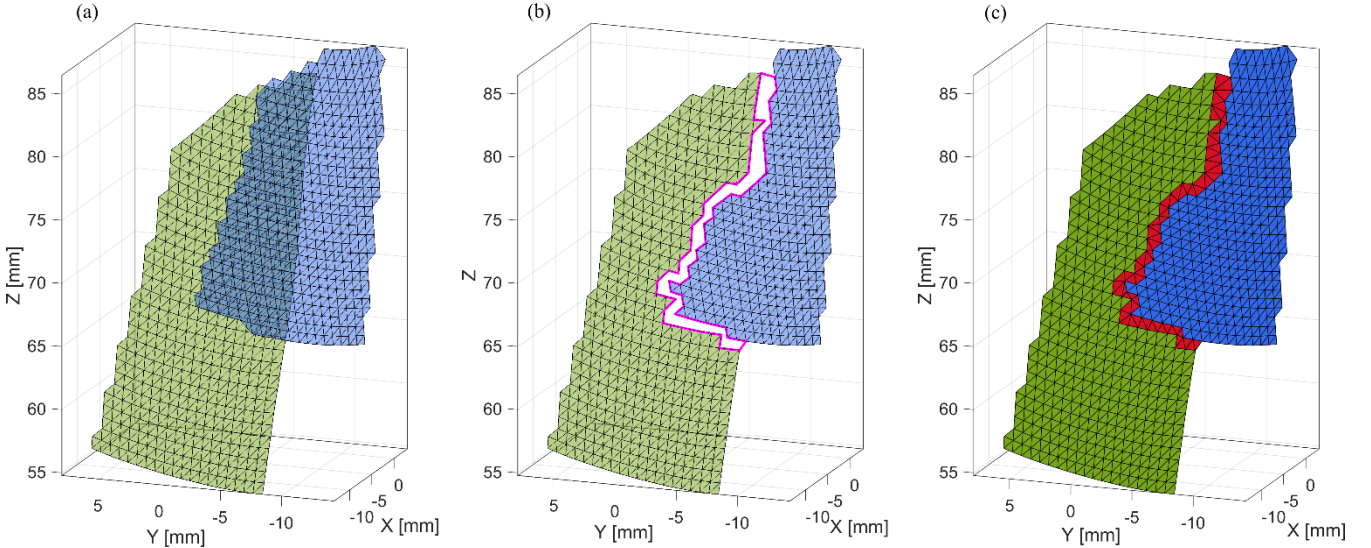


**FIGURE 4.** Surface merging example. (a) The green and blue 3D meshes were reconstructed from two adjacent camera-pairs. (b) The overlap regions are identified, and faces are removed from the boundaries until the overlap is resolved and a minimum gap exist between the surfaces. The gap which needs to be filled with new triangles is marked with a magenta line (c) The gap is filled with new triangular faces by locally applying Delaunay triangulation, using only vertices existing in the original data.

## G. POST-PROCESSING

In this step, the 3D coordinates of the triangular mesh's vertices in the reference and current configurations are used to derive the full-field displacement, deformation, and strain. For each triangular element and for each configuration, the deformation gradient tensor  $\mathbf{F}$  is calculated using a variation of the triangular Cosserat point element method [47], [48]. Assuming a homogenous deformation field within each element, this method obtains the finite (nonlinear) deformation field with the same spatial resolution as the DIC measurement, and independently from adjacent data points and numerical derivatives.

The reference configuration of a given triangular element is denoted by the position vectors  $\{\mathbf{P}_1, \mathbf{P}_2, \mathbf{P}_3\}$  of its three vertices, and the values of these position vectors in a current configuration are denoted by  $\{\mathbf{p}_1, \mathbf{p}_2, \mathbf{p}_3\}$ . Moreover, the reference and current configurations are characterized by the director vectors  $\{\mathbf{D}_1, \mathbf{D}_2, \mathbf{D}_3\}$  and  $\{\mathbf{d}_1, \mathbf{d}_2, \mathbf{d}_3\}$ , respectively, defined as

$$\begin{aligned}
\mathbf{D}_1 &= \mathbf{P}_2 - \mathbf{P}_1; \quad \mathbf{D}_2 = \mathbf{P}_3 - \mathbf{P}_1; \quad \mathbf{D}_3 = \frac{\mathbf{D}_1 \times \mathbf{D}_2}{|\mathbf{D}_1 \times \mathbf{D}_2|} \\
\mathbf{d}_1 &= \mathbf{p}_2 - \mathbf{p}_1; \quad \mathbf{d}_2 = \mathbf{p}_3 - \mathbf{p}_1; \quad \mathbf{d}_3 = \frac{\mathbf{d}_1 \times \mathbf{d}_2}{|\mathbf{d}_1 \times \mathbf{d}_2|} \\
\mathbf{D}_1 \times \mathbf{D}_2 \cdot \mathbf{D}_3 &= 2A,
\end{aligned} \tag{12}$$

such that  $\mathbf{D}_3$  and  $\mathbf{d}_3$  are unit vectors normal to the plane of the triangle in its reference and current configurations, respectively, and  $A$  is the triangle's reference area. Then, the reference reciprocal vectors  $\{\mathbf{D}^1, \mathbf{D}^2, \mathbf{D}^3\}$  are defined by

$$\begin{aligned}
\mathbf{D}^1 &= \frac{\mathbf{D}_2 \times \mathbf{D}_3}{2A}; \quad \mathbf{D}^2 = \frac{\mathbf{D}_3 \times \mathbf{D}_1}{2A}; \\
\mathbf{D}^3 &= \frac{\mathbf{D}_1 \times \mathbf{D}_2}{2A} = \mathbf{D}_3,
\end{aligned} \tag{13}$$

such that  $\mathbf{D}^i \cdot \mathbf{D}_j = \delta_j^i$ , where  $\delta_j^i$  is the Kronecker delta symbol. Consequently, the deformation gradient tensor  $\mathbf{F}$  is defined by

$$\mathbf{F} = \sum_{i=1}^3 \mathbf{d}_i \otimes \mathbf{D}^i, \tag{14}$$

where  $\otimes$  is the tensor (outer) product.  $\mathbf{F}$  transforms any material line in the triangular element from the reference to the current configuration, including the director vectors and the principal directions, such that it satisfies

$$\begin{aligned}
\mathbf{d}_i &= \mathbf{F} \mathbf{D}_i \\
\mathbf{n}_i &= \mathbf{F} \mathbf{N}_i.
\end{aligned} \tag{15}$$

Next, the right and left Cauchy-Green deformation tensors ( $\mathbf{C}$  and  $\mathbf{B}$ , respectively), and the associated Green-Lagrangian and Eulerian-Almansi finite strain tensors ( $\mathbf{E}$  and  $\mathbf{e}$ , respectively), are defined by

$$\begin{aligned}
\mathbf{C} &= \mathbf{F}^T \mathbf{F}; \quad \mathbf{B} = \mathbf{F} \mathbf{F}^T \\
\mathbf{E} &= \frac{1}{2}(\mathbf{C} - \mathbf{I}); \quad \mathbf{e} = \frac{1}{2}(\mathbf{I} - \mathbf{B}^{-1}),
\end{aligned} \tag{16}$$

where  $\mathbf{I}$  is the unity second order tensor. Moreover, the spectral decompositions of these tensors are given by

$$\begin{aligned}
\mathbf{C} &= \lambda_1^2(\mathbf{N}_1 \otimes \mathbf{N}_1) + \lambda_2^2(\mathbf{N}_2 \otimes \mathbf{N}_2) + \lambda_3^2(\mathbf{N}_3 \otimes \mathbf{N}_3) \\
\mathbf{B} &= \lambda_1^2(\mathbf{n}_1 \otimes \mathbf{n}_1) + \lambda_2^2(\mathbf{n}_2 \otimes \mathbf{n}_2) + \lambda_3^2(\mathbf{n}_3 \otimes \mathbf{n}_3) \\
\mathbf{E} &= E_1(\mathbf{N}_1 \otimes \mathbf{N}_1) + E_2(\mathbf{N}_2 \otimes \mathbf{N}_2) + E_3(\mathbf{N}_3 \otimes \mathbf{N}_3) \\
\mathbf{e} &= e_1(\mathbf{n}_1 \otimes \mathbf{n}_1) + e_2(\mathbf{n}_2 \otimes \mathbf{n}_2) + e_3(\mathbf{n}_3 \otimes \mathbf{n}_3),
\end{aligned} \tag{17}$$

where  $\lambda_i$  are the principal stretches,  $\mathbf{N}_i$  and  $\mathbf{n}_i$  are the principal directions in the reference and current configurations, and  $E_i$  and  $e_i$  are the principal Green-Lagrangian and Euler-Almansi strains, respectively. Since each triangular element is planar, one of the principal stretches must equal to one (e.g.  $\lambda_3 = 1$ ), and one of the principal strains must equal to zero (e.g.  $E_3 = e_3 = 0$ ). Furthermore, their associated directions are normal to the triangle's surface ( $\mathbf{N}_3 = \mathbf{D}_3$  and  $\mathbf{n}_3 = \mathbf{d}_3$ ). It is noted that although strains are more commonly presented, stretches are often preferred in the case of large deformation, since their definition is unique, while numerous strain definitions exist besides the ones described above (e.g. Seth-Hill class strains [49], [50] and Bazant strains [51]).

Furthermore, the dilatation  $J$ , which corresponds to the relative surface area change of the triangle, is given by

$$J = \det(\mathbf{F}) = \lambda_1 \lambda_2. \tag{18}$$

When the deformation includes large motion, it is often desirable to subtract the average RBM such that the deformation can be visualized without large movement of the object. Therefore, the average RBM is estimated for each configuration using the least-squares minimization approach (rigid superimposition) [52], [53].

MultiDIC offers functions for the dynamic visualization of the displacements, stretches and strains (magnitude and direction), surface area change, as well as additional measures such as the correlation coefficient and the color texture from the original images.

#### H. EXPERIMENTAL SETUP

A 360° stereo camera rig was designed and fabricated, to hold up to 30 cameras (Raspberry Pi Camera Module V2, featuring a Sony IMX219 8-megapixel  $3.674 \times 2.760 \text{ mm}^2$  CMOS sensor, connected to Raspberry Pi Zero-w) in a 700 mm diameter circle, as shown in Fig. 5. The objects to be imaged were placed in the center of the circle where it could be uniformly illuminated by circular arrays of flexible LED strips. All cameras were connected through an Ethernet hub and synchronously controlled using a PC. For the experiments described in this paper, twelve cameras were placed coaxially, resulting in twelve stereo-pairs with an angular displacement of 30°, such that the distance between each pair of contiguous cameras was about 181 mm. This stereo-angle is small enough to provide both a sufficient overlapping portion and an acceptable level of distortion between image-pairs, and at the same time large enough to allow for accurate out-of-plane displacement measurements [19], [20]. The system was very low-cost (<\$1,000 total, including 12 cameras, cables, LEDs, Ethernet hub, power supplies, and building materials for the rig). A 3D calibration object was prepared by accurately lathing a 250 mm long, 114 mm diameter aluminum cylinder, to achieve a uniform diameter throughout the cylinder's length. This cylinder was then wrapped in a white adhesive paper with a printed grid pattern of black square dots (4 mm by 4 mm squares, 12 mm spacing), as shown in Fig. 5 (a).

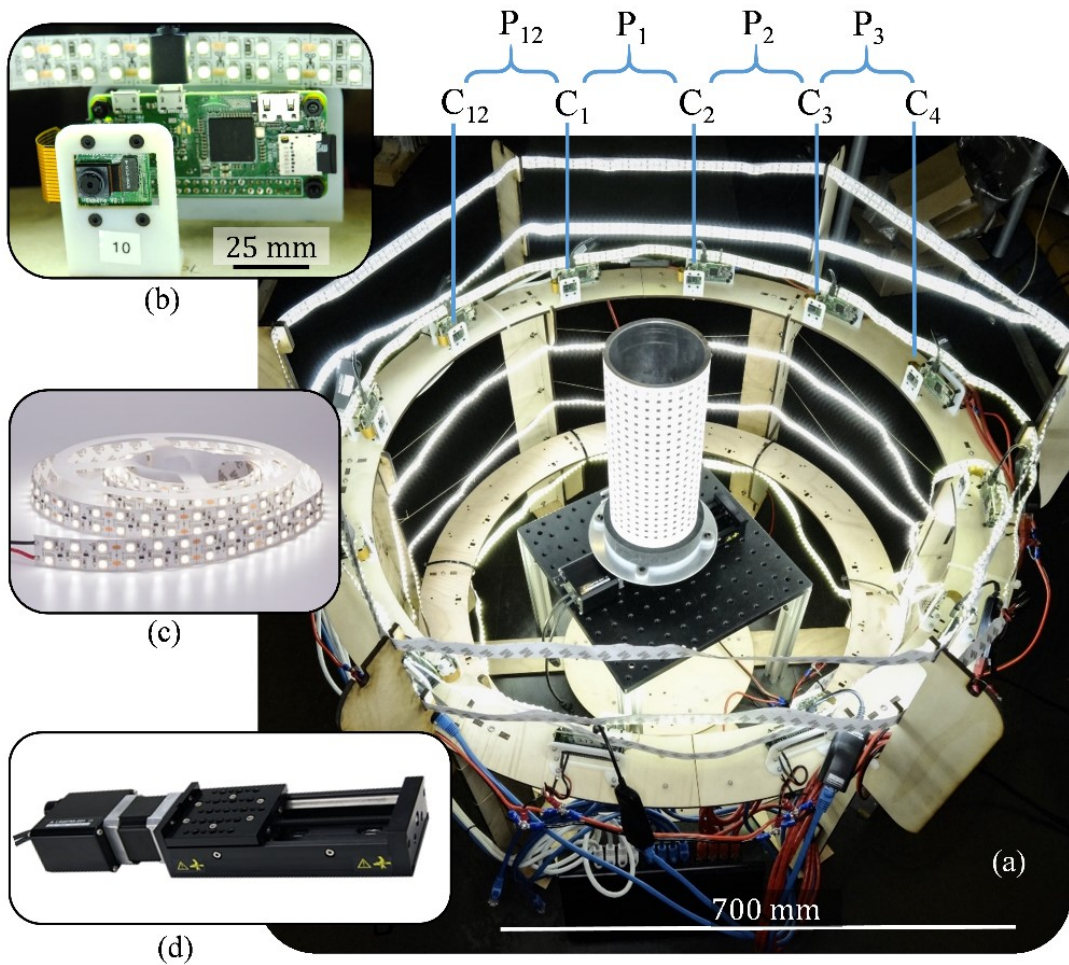


**FIGURE 5.** Experimental setup. (a) The 360° rig holding 12 Raspberry Pi camera units, one of which is shown enlarged in (b). Each pair of adjacent cameras  $[C_1, C_2]$ ,  $[C_2, C_3]$ ... $[C_{12}, C_1]$ , constitute a stereo-pair  $(P_1, P_2 \dots P_{12})$ . The calibration object is placed at the center of the rig and illuminated using flexible LED strips, which are shown enlarged in (c). A motorized translation stage (d) was placed under the calibration object for the validation experiments.

## I. METROLOGICAL PERFORMANCE ASSESSMENT

To evaluate the errors associated with stereo calibration independently of the DIC process, an experiment was performed, whereby the 3D positions of the centroids of the black dots on the calibration object were analyzed before and after a 5 mm displacement was applied with a motorized linear stage (Zaber Technologies A-LSQ075B-E01, max 0.5  $\mu\text{m}$  microstep error), as shown at the bottom of the cylinder in Fig. 5(a), and the in Fig. 5(d). The reconstructed 3D points were then superimposed into their reference positions by estimating the optimal RBM between them. The Euclidian distances between corresponding points represent the stereo calibration errors.

The next set of verification experiments involved a 3D speckled test object which was prepared by applying an adhesive paper with a speckle pattern (black 1.4 mm circles printed in a random pattern on white paper) to the aluminum cylinder (see Fig. 3). The cylinder's surface was imaged using the camera rig and analyzed using MultiDIC. The performance of the complete 3D-DIC algorithm and experimental system was evaluated by analyzing the accuracy of the reconstructed shape, the merging error between adjacent camera-pairs, the displacement error, and the strain error, as detailed below.

The accuracy of the shape measurement was evaluated by comparing the fitted diameter of the reconstructed cylinder to the diameter measured using a large-capacity caliper ( $\pm 0.01$  mm accuracy). Next, the merging errors between surfaces reconstructed by different camera-pairs were evaluated by reconstructing a portion of the surface visible by three adjacent cameras (such as the overlapping region illustrated in Fig. 1). The center camera ( $C_2$ ) was defined as the reference camera for the two pairs:  $[C_2, C_1]$  and  $[C_2, C_3]$ , such that the same reference point grid was used for both pairs. The 3D point clouds reconstructed by the two camera-pairs should theoretically be identical. Therefore, any distance between them represents a merging error.

Next, the speckled cylinder was translated using the motorized linear stage, in 10 steps of 0.1 mm increment, and the displacements errors were calculated by comparing the displacements measured using 3D-DIC and those measured using the stage. Moreover, the 3D strains, which should theoretically equal to zero, were analyzed to evaluate the overall accuracy of the strain measurement.

Finally, to demonstrate the capability of the proposed methods to measure *in-vivo* shapes and deformations, the surface of the lower limb of a human subject (healthy 34 y.o. female) was measured. A custom speckling stamp was made by laser-engraving a rubber sheet with the same speckle pattern described above. A uniform layer of white temporary tattoo ink (ProAiir, ShowOffs Body Art LLC., USA) was applied to the skin surface to enhance contrast and to create a homogenous background. Next, a speckle pattern was applied with black temporary tattoo ink (ProAiir, ShowOffs Body Art LLC., USA) using the stamp. The lower leg of the subject was imaged while the subject performed unconstrained ankle plantarflexion (from the most dorsiflexed position to the most plantar flexed position). The experimental procedure was approved by the Committee on the Use of Humans as Experimental Subjects of the Massachusetts Institute of Technology (COUHES protocol: 1101004280).

All the DIC analyses were performed using 20 pixels subset radius and 10 pixels step size at a  $\sim 10$  *pixel/mm* ratio. All the results represent raw data. No kind of filtering or smoothing procedures were applied.

## III. RESULTS

### A. CAMERA INTRINSIC PARAMETERS AND 3D RECONSTRUCTION ERRORS

Table 1 reports the mean  $\pm$  standard deviation (STD) of the intrinsic parameters calculated using the BA method for the twelve cameras. For each camera, 50 images of a flat checkerboard pattern with  $15 \times 20$  black and white  $10 \times 10$   $\text{mm}^2$  squares were acquired. The number of significant digits for each parameter is based on its estimation error, as computed by the BA algorithm. The distortion parameters calculated using the original images were used for correcting the distortion on the detected image points. The corrected points were then used again for estimating the parameters. Therefore, the distortion parameters in the right column of Table 1 represent the values of the residual distortion.

The values of the 3D reconstruction errors  $\varepsilon_M$  and  $\varepsilon_R$ , obtained for all camera-pairs using DLT with and without distortion correction, are reported in Table 2.

TABLE I  
STATISTICS OF THE ESTIMATED INTRINSIC PARAMETERS

Parameter	Original image	After distortion correction
$f_x$	$2611.7 \pm 5.8$	$2611.9 \pm 5.7$
$f_y$	$2615.4 \pm 5.6$	$2615.7 \pm 5.5$
$C_x$	$1246.5 \pm 34.5$	$1247.7 \pm 36.4$
$C_y$	$1627.7 \pm 16.9$	$1627.2 \pm 17.4$
$s$	$-1.37 \pm 0.37$	$-1.37 \pm 0.34$
$k_1$	$0.17862 \pm 0.01803$	$0.00002 \pm 0.0001$
$k_2$	$-0.295 \pm 0.167$	$0.002 \pm 0.001$
$k_3$	$-0.19 \pm 0.45$	$0.00 \pm 0.00$
$p_1$	$0.00015 \pm 0.00023$	$0.00004 \pm 0.00006$
$p_2$	$0.00068 \pm 0.00066$	$0.00009 \pm 0.00001$

TABLE II  
RECONSTRUCTION ERRORS FOR ALL CAMERA-PAIRS

Pair number	Camera numbers	With DC <sup>1</sup>		Without DC <sup>1</sup>	
		$\epsilon_M [mm]$	$\epsilon_R [mm]$	$\epsilon_M [mm]$	$\epsilon_R [mm]$
1	[1,2]	0.002	0.051	0.003	0.446
2	[2,3]	0.003	0.045	0.005	0.375
3	[3,4]	0.001	0.058	0.009	0.357
4	[4,5]	0.001	0.059	0.007	0.364
5	[5,6]	0.001	0.046	0.003	0.332
6	[6,7]	0.002	0.034	0.003	0.343
7	[7,8]	0.003	0.055	0.008	0.425
8	[8,9]	0.002	0.041	0.006	0.366
9	[9,10]	0.002	0.042	0.003	0.345
10	[10,11]	0.002	0.042	0.004	0.338
11	[11,12]	0.001	0.054	0.003	0.414
12	[12,1]	0.003	0.038	0.006	0.442
All cameras		0.002	0.047	0.005	0.379

<sup>1</sup>DC = Distortion Correction

### B. STEREO CALIBRATION TEST

Fig. 6 reports the stereo calibration errors, represented by the Euclidian distances between corresponding points of the calibration object measured in two configurations and rigidly superimposed. Fig. 6(a) illustrates the error magnitudes of individual points, and Fig. 6(b) summarizes the statistics of the 3D components of the errors obtained with and without distortion correction. The mean errors were very small both with and without distortion correction ( $\sim 10^{-14}$  mm), but the RMS of the error magnitudes was smaller when the distortion correction was employed (0.017 mm) than when it was not employed (0.026 mm).

### B. 3D-DIC TESTS OF A RIGID SPECKLED OBJECT

The errors reported in this section are associated with the entire 3D-DIC procedure. The correctness of the shape measurement was evaluated by comparing the fitted diameter of the reconstructed cylinder to the 114.00 mm diameter (including the adhesive paper) measured using the caliper. The mean  $\pm$  STD of the diameter measured using 3D-DIC was  $113.93 \pm 0.27$  and  $113.91 \pm 0.56$  mm, with and without distortion correction, respectively.

The merging errors between surfaces reconstructed by two different camera-pairs are shown in Fig. 7(a). The reconstructed points are plotted with colors depicting the magnitude of the Euclidean distance between the two sets. The mean  $\pm$  STD of the

errors were  $0.06 \pm 0.03$  mm and  $0.08 \pm 0.06$  mm, with and without distortion correction, respectively. As expected, the distortion correction improved the merging accuracy mostly in the ROI's upper and lower ends, corresponding to the marginal areas of the images.

The displacements and displacement errors are summarized in Fig. 7(b) (top and center) as a function of the imposed displacement. Fig. 7(c) shows the strain magnitude distribution over half of the cylinder, for the 0.5 mm displacement step, while the statistics for all displacement steps are summarized in Fig. 7(b) (bottom).

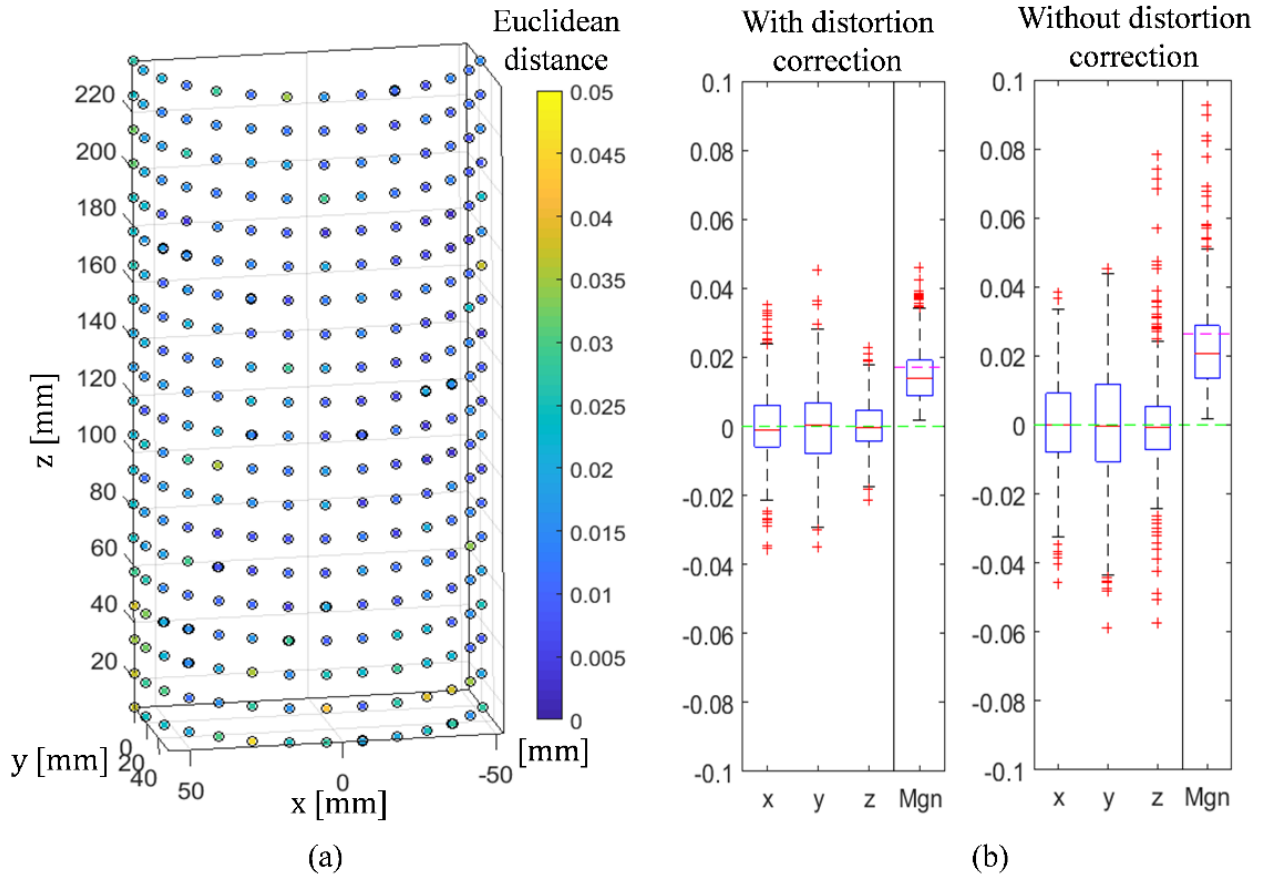


**FIGURE 6.** Stereo calibration error analysis. Two sets of calibration object images (before and after 5 mm displacement) were analyzed. (a) The 3D positions of the control points on the calibration object, as reconstructed in the first set (black hollow circles), and their positions measured in the second (displaced) set superimposed into the first set (plotted with colors depicting the absolute distance between them). (b) The error statistics for all the control points, obtained with and without distortion correction, in the x, y, and z directions, and the error magnitude (*Mgn*). The boxplots report the median (red line), 25<sup>th</sup> and 75<sup>th</sup> quartiles (blue box), and outliers (red crosses). The green dashed line represents zero error, and the magenta dashed line represents the RMS error.

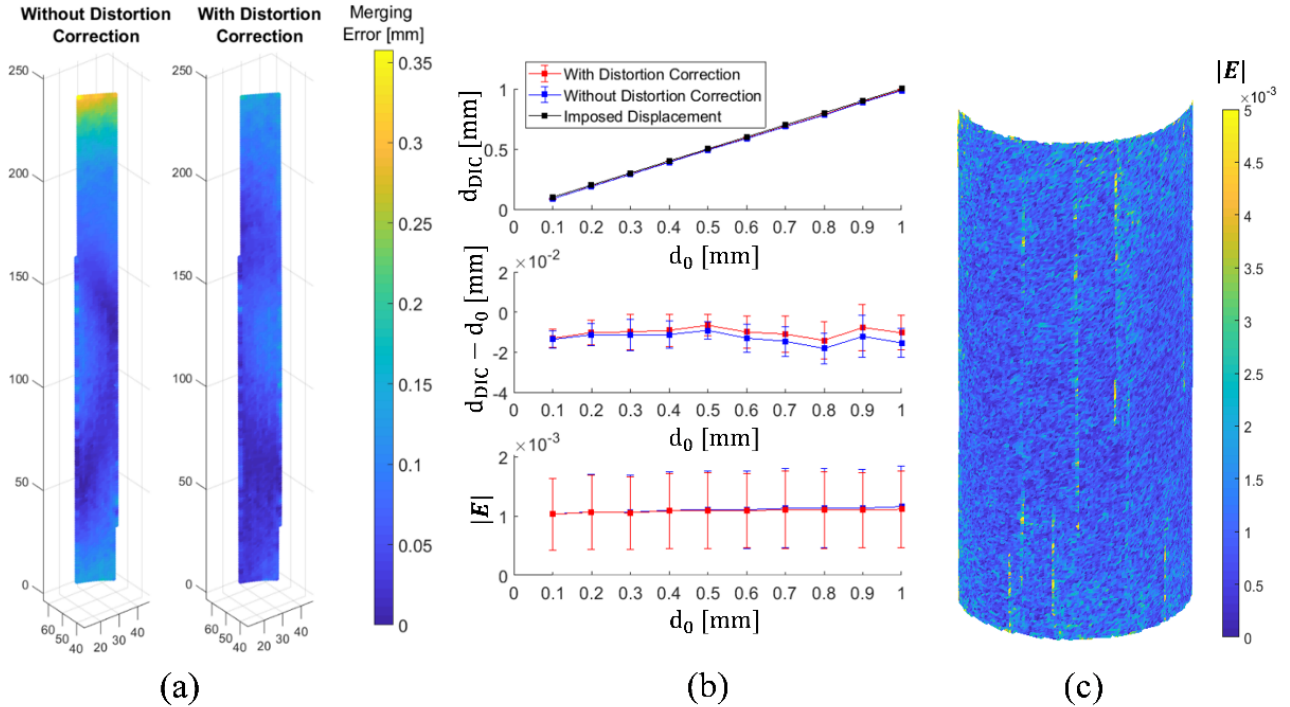


**FIGURE 7.** 3D-DIC results of a rigid speckled cylinder. (a) Merging error depicted as the Euclidian distance between the points reconstructed by two adjacent camera-pairs (such as the overlapping region in Fig. 1); (b) Results from a set of 10 imposed translations ( $d_0$ ) with a 0.1 mm increment. The measured displacements (top), displacement errors (center) and Green-Lagrangian strain magnitude (bottom) are plotted as error bars which represent  $\pm$  one STD over all data points; (c) The Green-Lagrangian strain magnitude distribution plotted on half of the cylinder, for the 0.5 mm displacement step.

### C. 3D-DIC IN-VIVO TEST OF A DEFORMABLE BODY SEGMENT

Illustrative results from the 3D-DIC *in-vivo* measurement are shown in Fig. 8. The full surface of the calf region of the lower leg was imaged five times while the subject performed ankle plantarflexion. Results of the first and the last configurations are illustrated in Figs. 8 and 9. Fig. 8 illustrates the 2D-DIC results for one stereo-pair. Fig. 8(a) shows the reference image, on which the point grid was defined. The images in Fig. 8(b-d) represent deformed states of (a). Note that the image distortion with respect to (a) is due to perspective in (b), due to deformation in (c), and due to perspective and deformation in (d). Fig. 9 plots the full surface reconstructed by 12 cameras in the reference (a) and deformed (b and c) configurations, which corresponds to the same configurations shown in Fig. 8. The colors on the surface depict the local values of the first and second principal stretches, and the black lines represent their directions, with lengths proportional to the stretch magnitude. Since (a) shows the reference configuration, the stretch values equal to one by definition, and no stretch direction are shown. The deformation fields are visibly smooth, despite the facts that it was computed independently on each triangular face and that no smoothing or filtering was applied to the raw data, contrarily to common DIC strain calculation schemes [1], [54]. Animated figures plotting the dynamic values of the displacement magnitude, the Lagrangian strain magnitude, the principal stretches, the surface area change, and the effect of RBM subtraction, are provided in the online Graphical Abstract video.

### IV. DISCUSSION

This paper describes the principal algorithms implemented in MultiDIC, a newly developed 3D-DIC MATLAB toolbox for multi-camera systems. The methods and system were designed to overcome some of the limitations involved with the calibration and data merging techniques commonly used in 3D-DIC. One primary advantage of MultiDIC is that it allows for a simple calibration process even when using a large number of cameras, without losing the ability to compensate for lens distortions. Consequently, the new method offers the flexibility of modifying the camera poses during experiments without requiring substantial additional re-calibration time.

The metrological capabilities of MultiDIC were validated by several experimental tests using a low-cost multi-camera setup. The errors associated with the proposed stereo calibration method were examined independently of the DIC procedure, by analyzing the 3D positions of the calibration object's control points in two configurations. The errors when using distortion

correction procedure were  $0.000 \pm 0.017$  mm (STD and RMS 35% lower than without distortion correction). These errors are relatively low considering the large size of the calibration object, and the cameras' large FOV and very low price.

Next, the metrological errors associated to the entire multi-view 3D-DIC procedure were evaluated by measuring the shape, displacement and strain error with a speckled cylindrical object. The shape measurements revealed errors smaller than 0.01 mm (<0.1%) in obtaining the cylinder's diameter. The merging errors and displacement errors were also found to be in the order of 0.01 mm, which is comparable to the stereo calibration errors. Furthermore, the strains measured as a result of RBM were in the range of  $10^{-3}$ , which is sufficiently accurate in our case, and is acceptable in most biomechanical applications, in which large deformations are involved. Moreover, this strain error is relatively low considering that, contrarily to commonly adopted DIC strain calculation schemes, no kinds of filtering and smoothing were applied to the raw data.

The MultiDIC toolbox and camera rig were utilized for *in-vivo* measurements to further illustrate capabilities of the system in clinical settings. It was shown that the dynamic behavior of the entire surface of the shank segment of a human subject can be reconstructed, that a smooth strain field can be obtained from the raw data, and that large deformations can be tracked. The results in Fig. 9 and in the online Graphical Abstract illustrate how the subject's lower limb shape changes due to the contraction of the calf muscles and the plantarflexion of the ankle joint. This test served as a proof of principle, and was not intended to provide any physiological or biomechanical finding.

The main limitation in this study is that the metrological performance tests were performed using very low-cost camera modules. Therefore, the accuracies reported here are adequate only for certain applications. However, the entire procedure is expected to outperform when high quality cameras and lenses are used. The use of low-cost hardware was motivated by the large number of cameras required, and was encouraged by previous studies which demonstrated the feasibility of using consumer-grade cameras [16], [55]. Future research could determine the performance of MultiDIC using high quality optics. Another limitation is that only one multi-view setup and calibration object was used in this study. However, the toolbox can be easily adapted to any multi-view setup, as long as a calibration object with a proper geometry is used.

It is noted that additional algorithms for 3D-DIC exist (e.g. [12]–[17], [56]), some of them offer significant advances. Moreover, an increasing number of DIC-related open-source tools is seen lately (e.g. [17], [38], [57]–[59]). In order to make these techniques more accessible and the results more reproducible, researchers are encouraged to extend the functionality of the toolbox by implementing additional algorithms as contributors [30], [60].

Future research by the authors will incorporate the tools established here in biomechanical studies, whereby the measured dynamic shapes of the residual limbs of lower-limb amputees will be used to inform the computational mechanical design of subject-specific optimized prosthetic sockets [61]. Moreover, the subject-specific soft-tissue mechanical properties will be evaluated, by analyzing simultaneous force/torque measurements and surface deformation measurements of the entire residual limb during *in-vivo* indentations. Then, the hyper-elastic and visco-elastic properties will be characterized using inverse finite element analysis [62], [63].

## V. CONCLUSION

This paper presents a newly developed open-source MATLAB toolbox for 3D-DIC, which implements algorithms specifically tailored for multi-camera applications, which are often desirable in biomechanics. Several verification tests have confirmed that accurate measurements can be achieved using MultiDIC and low-cost hardware. The development of a user-friendly, high-quality and freely available software, will greatly increase the availability of 3D-DIC to the scientific community. The capabilities to efficiently measure *in-vivo* skin shape and deformation were demonstrated, and future research will utilize these methods in various biomechanical studies.

## ACKNOWLEDGMENT

The authors would like to thank Dr. Lisa E. Freed for her valuable suggestions to the manuscript, Matthew E. Carney for his contribution to the graphical abstract, and the MIT Undergraduate Research Opportunity Program (UROP) students who assisted throughout the development and testing.

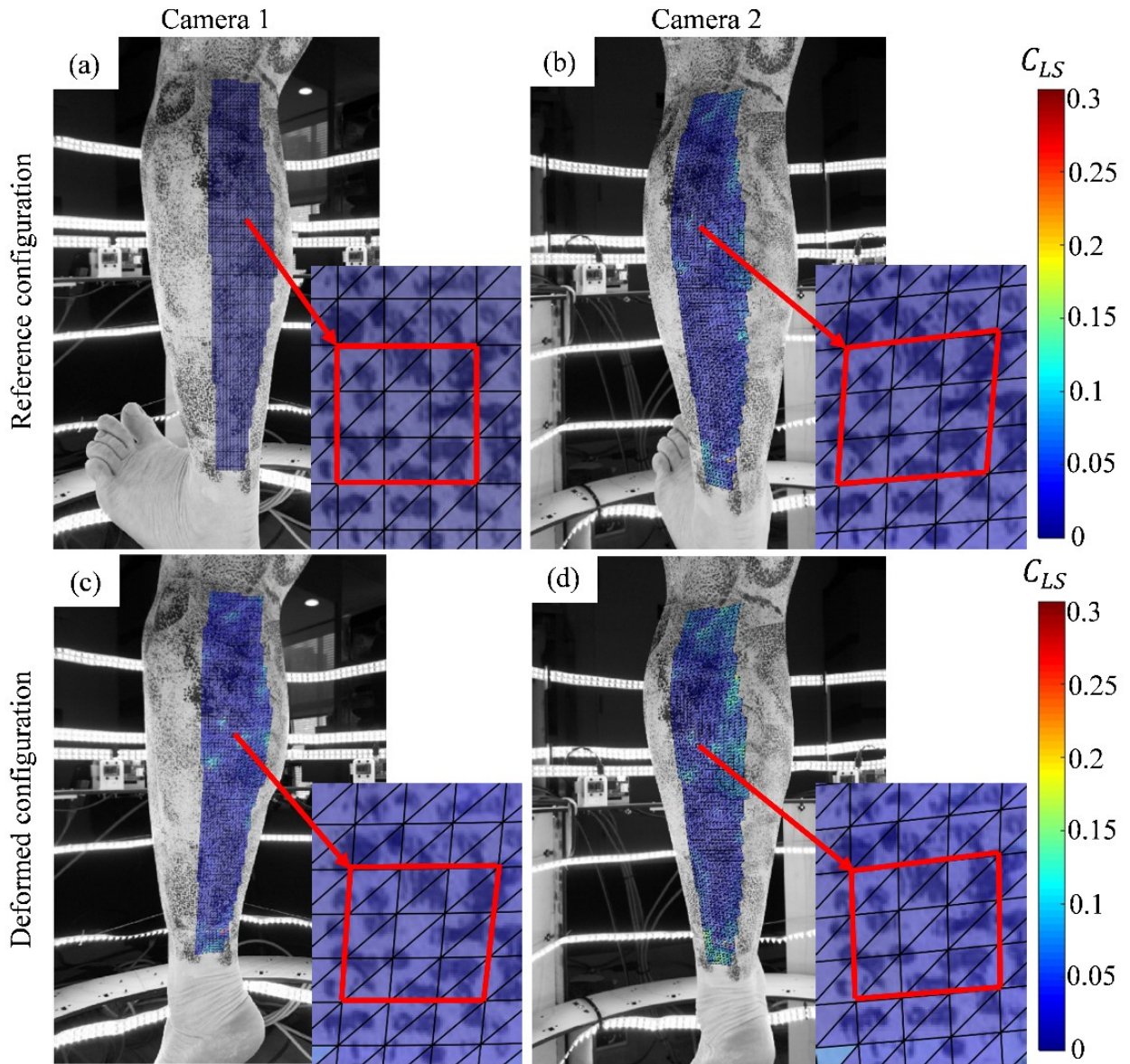


**FIGURE 8.** *In-vivo* body segment test – Correlation maps. Sub-figures (a)-(d) show images from adjacent cameras in the reference (a, b) and deformed (c, d) configurations. The ROI is plotted with colors depicting the correlation coefficient, and zoomed-in portions are enlarged in insets.

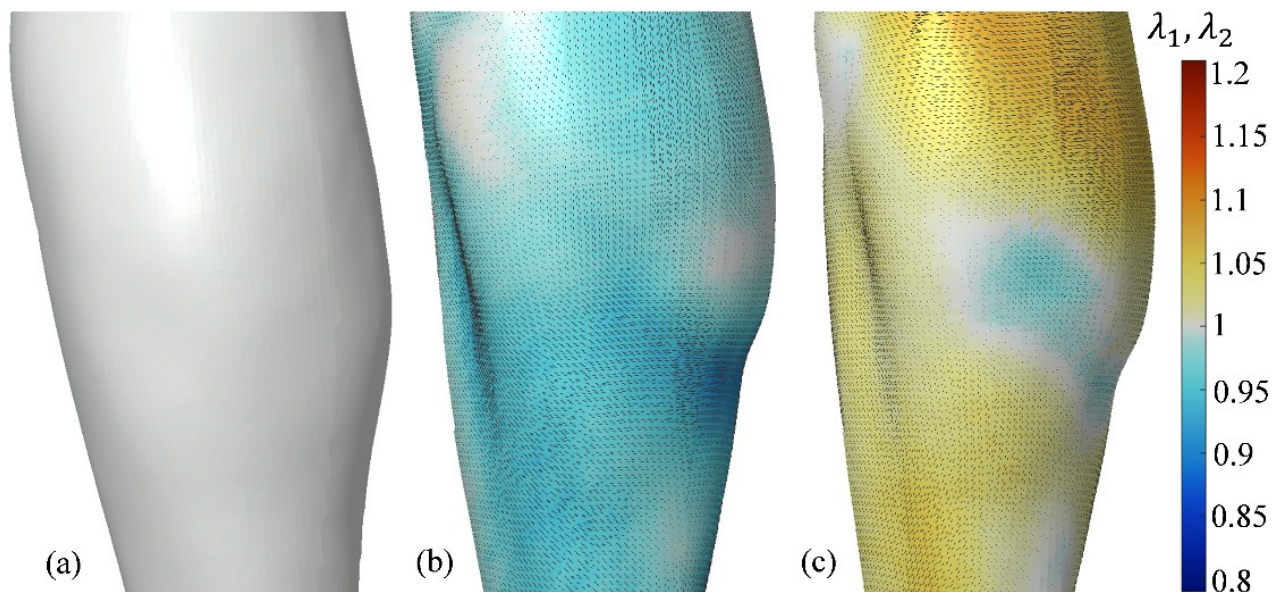


**FIGURE 9.** *In-vivo* body segment test – Deformations. The full 360° surface reconstructed from 12 cameras is shown in its reference (a) and deformed (b, c) configurations. The face colors depict the principal stretch values  $\lambda_1$  (b) and  $\lambda_2$  (c), and the black lines represent the principal directions  $N_1$  (b) and  $N_2$  (c). Lighting was added to better visualize the surface contours.

## REFERENCES

- [1] M. A. Sutton, J.-J. Orteu, and H. Schreier, *Image Correlation for Shape, Motion and Deformation Measurements*. Boston, MA: Springer US, 2009.
- [2] B. Pan, K. Qian, H. Xie, and A. Asundi, “Two-dimensional digital image correlation for in-plane displacement and strain measurement: a review,” *Meas. Sci. Technol.*, vol. 20, no. 6, p. 62001, Jun. 2009.
- [3] O. Faugeras, *Three-dimensional computer vision: a geometric viewpoint*. 1993.
- [4] F. Hild and S. Roux, “Digital Image Correlation: from Displacement Measurement to Identification of Elastic Properties - a Review,” *Strain*, vol. 42, no. 2, pp. 69–80, May 2006.
- [5] M. Palanca, G. Tozzi, and L. Cristofolini, “The use of digital image correlation in the biomechanical area: a review,” *Int. Biomech.*, vol. 3, no. 1, pp. 1–21, 2016.
- [6] K. Genovese, L. Casaletto, J. D. Humphrey, and J. Lu, “Digital image correlation-based point-wise inverse characterization of heterogeneous material properties of gallbladder in vitro,” *Proc. R. Soc. A Math. Phys. Eng. Sci.*, vol. 470, no. 2167, pp. 20140152–20140152, 2014.
- [7] P. Badel, S. Avril, S. Lessner, and M. Sutton, “Mechanical identification of layer-specific properties of mouse carotid arteries using 3D-DIC and a hyperelastic anisotropic constitutive model,” *Comput. Methods Biomech. Biomed. Engin.*, vol. 15, no. 1, pp. 37–48, Jan. 2012.
- [8] S. Avril, “Hyperelasticity of Soft Tissues and Related Inverse Problems,” in *Material Parameter Identification and Inverse Problems in Soft Tissue Biomechanics*, Springer, Cham, 2017, pp. 37–66.
- [9] A. S. Dickinson, A. C. Taylor, H. Ozturk, and M. Browne, “Experimental validation of a finite element model of the proximal femur using digital image correlation and a composite bone model,” *J. Biomech. Eng.*, vol. 133, no. January, p. 14504, 2011.
- [10] R. Maiti *et al.*, “In vivo measurement of skin surface strain and sub-surface layer deformation induced by natural tissue stretching,” *J. Mech. Behav. Biomed. Mater.*, vol. 62, pp. 556–569, 2016.
- [11] K. Ito *et al.*, “Dynamic measurement of surface strain distribution on the foot during walking,” *J. Mech. Behav. Biomed. Mater.*, vol. 69, no. December 2016, pp. 249–256, 2017.
- [12] Y. Gao, T. Cheng, Y. Su, X. Xu, Y. Zhang, and Q. Zhang, “High-efficiency and high-accuracy digital image correlation for three-dimensional measurement,” *Opt. Lasers Eng.*, vol. 65, pp. 73–80, Feb. 2015.
- [13] K. Genovese and D. Sorgente, “A morphing-based scheme for large deformation analysis with stereo-DIC,” *Opt. Lasers Eng.*, vol. 104, pp. 159–172, 2017.
- [14] L. Wittevrongel, P. Lava, S. V. Lomov, and D. Debruyne, “A Self Adaptive Global Digital Image Correlation Algorithm,” *Exp. Mech.*, vol. 55, no. 2, pp. 361–378, Feb. 2015.
- [15] M. A. Sutton *et al.*, “Recent Progress in Digital Image Correlation: Background and Developments since the 2013 W M Murray Lecture,” *Exp. Mech.*, vol. 57, no. 1, pp. 1–30, Jan. 2017.
- [16] B. Pan, L. Yu, and D. Wu, “High-accuracy 2D digital image correlation measurements using low-cost imaging lenses: implementation of a generalized compensation method,” *Meas. Sci. Technol.*, vol. 25, no. 2, p. 25001, 2014.
- [17] A. K. Landauer, M. Patel, D. L. Henann, and C. Franck, “A q-Factor-Based Digital Image Correlation Algorithm (qDIC) for Resolving Finite Deformations with Degenerate Speckle Patterns,” *Exp. Mech.*, pp. 1–16, Mar. 2018.
- [18] P. L. Reu *et al.*, “DIC Challenge: Developing Images and Guidelines for Evaluating Accuracy and Resolution of 2D Analyses,” *Exp. Mech.*, Dec. 2017.
- [19] Y. Q. Wang, M. A. Sutton, X. D. Ke, H. W. Schreier, P. L. Reu, and T. J. Miller, “On Error Assessment in Stereo-based Deformation Measurements,” *Exp. Mech.*, vol. 51, no. 4, pp. 405–422, 2011.
- [20] X. D. Ke, H. W. Schreier, M. A. Sutton, and Y. Q. Wang, “Error Assessment in Stereo-based Deformation Measurements. Part II: Experimental

- Validation of Uncertainty and Bias Estimates,” *Exp. Mech.*, vol. 51, pp. 423–441, Apr. 2011.
- [21] M. A. Sutton and F. Hild, “Recent Advances and Perspectives in Digital Image Correlation,” *Exp. Mech.*, vol. 55, no. 1, pp. 1–8, Jan. 2015.
- [22] E. W. Obropta and D. J. Newman, “Skin strain fields at the shoulder joint for mechanical counter pressure space suit development,” *IEEE Aerosp. Conf. Proc.*, vol. 2016–June, pp. 1–9, 2016.
- [23] M. Hokka, N. Mirow, H. Nagel, M. Iqrsusi, S. Vogt, and V.-T. Kuokkala, “In-vivo deformation measurements of the human heart by 3D Digital Image Correlation,” *J. Biomech.*, vol. 48, no. 10, pp. 2217–2220, Jul. 2015.
- [24] Y. Wang, P. Lava, S. Coppiters, P. V. Houtte, and D. Debruyne, “Application of a multi-camera stereo DIC set-up to assess strain fields in an Erichsen test: Methodology and validation,” *Strain*, vol. 49, no. 2, pp. 190–198, 2013.
- [25] K. Genovese, L. Cortese, M. Rossi, and D. Amodio, “A 360-deg Digital Image Correlation system for materials testing,” *Opt. Lasers Eng.*, vol. 82, pp. 127–134, 2016.
- [26] J.-J. Orteu, F. Bugarin, J. Harvent, L. Robert, and V. Velay, “Multiple-Camera Instrumentation of a Single Point Incremental Forming Process Pilot for Shape and 3D Displacement Measurements: Methodology and Results,” *Exp. Mech.*, vol. 51, no. 4, pp. 625–639, Apr. 2011.
- [27] M. Malesa *et al.*, “Non-destructive testing of industrial structures with the use of multi-camera Digital Image Correlation method,” *Eng. Fail. Anal.*, vol. 69, pp. 122–134, Nov. 2016.
- [28] J. E. Dufour, F. Hild, and S. Roux, “Shape, displacement and mechanical properties from isogeometric multiview stereocorrelation,” *J. Strain Anal. Eng. Des.*, vol. 50, no. 7, pp. 470–487, 2015.
- [29] F. Chen, X. Chen, X. Xie, X. Feng, and L. Yang, “Full-field 3D measurement using multi-camera digital image correlation system,” *Opt. Lasers Eng.*, vol. 51, no. 9, pp. 1044–1052, 2013.
- [30] A. Erdemir *et al.*, “Perspectives on Sharing Models and Related Resources in Computational Biomechanics Research,” *J. Biomech. Eng.*, vol. 140, no. 2, p. 24701, Jan. 2017.
- [31] Y. I. Abdel-Aziz, “Direct linear transformation from comparator coordinates in close-range photogrammetry,” in *Proceedings American society of photogrammetry symposium on close-range photogrammetry*, 1971, pp. 1–19.
- [32] B. Triggs, P. F. McLauchlan, R. I. Hartley, and A. W. Fitzgibbon, “Bundle Adjustment — A Modern Synthesis,” Springer, Berlin, Heidelberg, 2000, pp. 298–372.
- [33] P. L. Reu, “A Study of the Influence of Calibration Uncertainty on the Global Uncertainty for Digital Image Correlation Using a Monte Carlo Approach,” *Exp. Mech.*, vol. 53, no. 9, pp. 1661–1680, Nov. 2013.
- [34] Correlated Solutions Inc., “CSI Application Note AN-722 Cylinder Data With Vic-3D.” [Online]. Available: <http://www.correlatedsolutions.com/supportcontent/cylinder-data-stitching.pdf>. [Accessed: 24-Jan-2018].
- [35] J. Heikkilä and O. Silven, “A four-step camera calibration procedure with implicit image correction,” *Proc. IEEE Comput. Soc. Conf. Comput. Vis. Pattern Recognit.*, pp. 1106–1112, 1997.
- [36] J. Weng, P. Cohen, and M. Herniou, “Camera calibration with distortion models and accuracy evaluation,” *IEEE Trans. Pattern Anal. Mach. Intell.*, vol. 14, no. 10, pp. 965–980, 1992.
- [37] G. Besnard, J. M. Lagrange, F. Hild, S. Roux, and C. Voltz, “Characterization of necking phenomena in high-speed experiments by using a single camera,” *Eurasip J. Image Video Process.*, no. 1, pp. 1–15, 2010.
- [38] J. Blaber, B. Adair, and A. Antoniou, “Ncorr: Open-Source 2D Digital Image Correlation Matlab Software,” *Exp. Mech.*, vol. 55, no. 6, pp. 1105–1122, 2015.
- [39] “What Is Camera Calibration? - MATLAB & Simulink.” [Online]. Available: <https://www.mathworks.com/help/vision/ug/camera-calibration.html>.
- [40] K. M. Moerman, “GIBBON: The Geometry and Image-Based Bioengineering add-On,” *J. Open Source Softw.*, vol. 3, no. 22, p. 506, 2018.
- [41] J. Bouguet, “Camera Calibration Toolbox for Matlab.” [Online]. Available: [http://www.vision.caltech.edu/bouguetj/calib\\_doc/](http://www.vision.caltech.edu/bouguetj/calib_doc/). [Accessed: 25-Jan-2018].
- [42] Z. Zhang, “A Flexible New Technique for Camera Calibration (Technical Report),” *IEEE Trans. Pattern Anal. Mach. Intell.*, vol. 22, no. 11, pp. 1330–1334, 2000.
- [43] G. Bradski and A. Kaehler, *Learning OpenCV*, First Edition. O’Reilly Media, Inc., 2008.
- [44] S. Baker and I. Matthews, “Lucas-Kanade 20 Years On: A Unifying Framework,” *Int. J. Comput. Vis.*, vol. 56, no. 3, pp. 221–255, Feb. 2004.
- [45] B. Pan, “Reliability-guided digital image correlation for image deformation measurement,” *Appl. Opt.*, vol. 48, no. 8, p. 1535, Mar. 2009.
- [46] H. Lu and P. D. Cary, “Deformation measurements by digital image correlation: Implementation of a second-order displacement gradient,” *Exp. Mech.*, vol. 40, no. 4, pp. 393–400, Dec. 2000.
- [47] D. Solav, M. B. Rubin, A. Cereatti, V. Camomilla, and A. Wolf, “Bone Pose Estimation in the Presence of Soft Tissue Artifact Using Triangular Cosserat Point Elements,” *Ann. Biomed. Eng.*, vol. 44, no. 4, pp. 1181–1190, Apr. 2016.
- [48] D. Solav, H. Meric, M. B. Rubin, D. Pradon, F. Lofaso, and A. Wolf, “Chest Wall Kinematics Using Triangular Cosserat Point Elements in Healthy and Neuromuscular Subjects,” *Ann. Biomed. Eng.*, vol. 45, no. 8, pp. 1963–1973, Aug. 2017.
- [49] B. R. Seth, “Generalized strain measure with applications to physical problems,” *MRC Tech. Summ. Rep. #248*, no. 248, pp. 1–18, 1961.
- [50] R. Hill, “On constitutive inequalities for simple materials-II,” *J. Mech. Phys. Solids*, vol. 16, no. 5, pp. 315–322, Aug. 1968.
- [51] Z. P. Bažant, “Easy-to-Compute Tensors With Symmetric Inverse Approximating Hencky Finite Strain and Its Rate,” *J. Eng. Mater. Technol.*, vol. 120, no. 2, p. 131, Apr. 1998.
- [52] M. B. Rubin and D. Solav, “Unphysical properties of the rotation tensor estimated by least squares optimization with specific application to biomechanics,” *Int. J. Eng. Sci.*, vol. 103, pp. 11–18, Jun. 2016.
- [53] D. Solav, M. B. Rubin, and A. Wolf, “Soft Tissue Artifact compensation using Triangular Cosserat Point Elements (TCPEs),” *Int. J. Eng. Sci.*, vol. 85, pp. 1–9, Dec. 2014.
- [54] P. Reu, “Virtual Strain Gage Size Study,” *Exp. Tech.*, vol. 39, no. 5, pp. 1–3, Sep. 2015.
- [55] L. Yu and B. Pan, “In-plane displacement and strain measurements using a camera phone and digital image correlation,” *Opt. Eng.*, vol. 53, no. 5, p. 54107, 2014.
- [56] H. Nguyen, H. Kieu, Z. Wang, and H. N. D. Le, “Three-dimensional facial digitization using advanced digital image correlation,” *Appl. Opt.*, vol. 57, no. 9, p. 2188, Mar. 2018.
- [57] D. Turner, “Digital Image Correlation Engine (DICE) Reference Manual.” Sandia Report, 2015.
- [58] F. Sur, B. Blaysat, and M. Grédiac, “Rendering Deformed Speckle Images with a Boolean Model,” *J. Math. Imaging Vis.*, pp. 1–17, Dec. 2017.
- [59] J. B. Estrada and C. Franck, “Intuitive Interface for the Quantitative Evaluation of Speckle Patterns for Use in Digital Image and Volume Correlation Techniques,” *J. Appl. Mech.*, vol. 82, no. 9, p. 95001, Sep. 2015.
- [60] R. D. Peng, “Reproducible research in computational science,” *Science*, vol. 334, no. 6060, pp. 1226–7, Dec. 2011.
- [61] K. M. Moerman, D. Senghe, and H. Herr, “Automated and Data-driven Computational Design of Patient-Specific Biomechanical Interfaces,” 2016.
- [62] K. M. Moerman, C. A. Holt, S. L. Evans, and C. K. Simms, “Digital image correlation and finite element modelling as a method to determine mechanical properties of human soft tissue in vivo,” *J. Biomech.*, vol. 42, no. 8, pp. 1150–1153, 2009.

- [63] D. M. Sengeh, K. M. Moerman, A. Petron, and H. M. Herr, "Multi-material 3-D viscoelastic model of a transtibial residuum from in-vivo indentation and MRI data," *J. Mech. Behav. Biomed. Mater.*, vol. 59, pp. 379–392, Feb. 2016.